Dependence of Northern Hemisphere Tropospheric Transport on the Midlatitude Jet under Abrupt CO_2 Increase

X. Zhang[1], D. W. Waugh[1], and C. Orbe[2,3]

[1]Department of Earth and Planetary Sciences, Johns Hopkins University, Baltimore, MD, USA.

[2]NASA Goddard Institute for Space Studies, New York, NY, USA.

[3]Department of Applied Physics and Applied Mathematics, Columbia University, New York, NY, USA

Corresponding author: Xiyue Zhang (sallyz@jhu.edu)

Key Points:

- Response of tropospheric tracer transport from the NH midlatitude surface to increased CO_2 depends on the midlatitude jet response.
- Changes in isentropic eddy mixing associated with the midlatitude jet dominate the response of the transport to NH high latitudes.
- A poleward shift of the NH midlatitude jet associated with AMOC weakening leads to less tracer in the midlatitudes and more in the Arctic.

Abstract

Understanding how the transport of gases and aerosols responds to climate change is necessary for policy making and emission controls. There is considerable spread in model projections of tracer transport in climate change simulations, largely because of the substantial uncertainty in projected changes in the large-scale atmospheric circulation. In particular, a relationship between the response of tropospheric transport into the high latitudes and a shift of the midlatitude jet has been previously established in an idealized modeling study. To test the robustness of this relationship, we analyze the response of a passive tracer of northern midlatitude surface origin to abrupt $2xCO_2$ and $4xCO_2$ in a comprehensive climate model (GISS E2.2-G). We show that a poleward shift of the northern midlatitude jet and enhanced eddy mixing along isentropes on the poleward flank of the jet result in decreased tracer concentrations over the midlatitudes and increased concentrations over the Arctic. This mechanism is robust in abrupt $2xCO_2$ and $4xCO_2$ simulations, the nonlinearity to CO_2 forcing, and two versions of the model with different atmospheric chemistry. Preliminary analysis of realistic chemical tracers suggests that the same mechanism can be used to provide insights into the climate change response of anthropogenic pollutants.

Plain Language Summary

Pollutants such sulfate aerosols, soot, and carbon monoxide are transported by atmospheric flows from the northern midlatitude surface to higher altitudes and the Arctic. Here we study how this transport responds to climate change by using a passive tracer without chemistry. During northern winter, the westerly jet accelerates and shifts poleward under increased CO_2 concentration. This leads to more mixing that brings cleaner air from the subtropical surface to the midlatitude troposphere but also polluted air from the midlatitude surface to the Arctic troposphere. This pattern is robust in tracers with and without chemistry, suggesting that transport changes play an important role in shaping the response of pollutant distributions to climate change. It also suggests that reducing the uncertainty of the midlatitude jet response will facilitate more accurate projection of pollutant transport in a warming climate.

1 Introduction

The long-range transport of trace gases and aerosols from the surface throughout the troposphere plays a key role in determining the composition of the atmosphere, climate change, and air quality. It is therefore important to know the processes controlling this transport and how the transport will change with climate. Previous studies comparing simulations of real and idealized tracers show a large spread among models (Shindell et al., 2008; Monks et al., 2015; Orbe et al., 2017, 2018; Yang et al., 2019). Furthermore, there remain large uncertainties in the role of different processes in causing changes, such as the relative role of changes in the large-scale circulation, isentropic mixing, and convection (e.g., Orbe et al., 2018; Yang et al., 2019). In addition, there is a large spread among model projections of transport in climate change simulations (e.g., Doherty et al., 2017).

This uncertainty in future changes in tracer transport is not surprising as there is substantial uncertainty in projections of the atmospheric circulation response to increasing greenhouse gas concentrations (e.g., Shepherd, 2014). For example, while models generally predict a poleward shift in the westerly jet (which has been linked to changes in transport, e.g., Orbe et al., 2013, 2015), there is a large spread among models in the magnitude of this shift (e.g., Vallis et al., 2015; Grise & Polvani, 2016; Oudar et al., 2020) and this spread is not correlated with the level of global warming in the models (Grise & Polvani, 2016).

Using a dry dynamical core model and air-mass fraction tagging, Orbe et al. (2013) analyzed changes in tropospheric transport to idealized warming. They found an increase in the fraction of air originating from the northern hemisphere (NH) extratropical (north of 33°N) boundary layer in the high-latitude upper troposphere. They attributed this increase to a poleward shift of the NH midlatitude jet resulting in enhanced eddy kinetic energy (EKE) that stirs more air out of the midlatitude boundary layer in a warmer climate. We are motivated to test the robustness of the relationship between midlatitude jet/EKE responses and changes in tropospheric transport.

The climate change response in Orbe et al. (2013) features upper tropospheric warming, which is a known mechanism to drive a poleward shift of the midlatitude jet via strengthened meridional temperature gradients. However, comprehensive climate models also simulate NH high latitude warming associated with Arctic amplification that weakens the meridional

temperature gradient. The resulting NH jet shift represents a "tug-of-war" between the two opposing temperature responses (Shaw et al., 2016; Shaw, 2019). A further complication is the temperature response in the North Atlantic, namely the presence of the North Atlantic warming hole (NAWH) that can result from the slowdown of the Atlantic Meridional Overturning Circulation (AMOC, e.g., Rahmstorf et al., 2015), changes in oceanic heat transport (Drijfhout et al., 2012; Keil et al., 2020), and increased local westerlies (He et al., 2022). Differences in NAWH can lead to a nonlinear climate change response to CO_2 forcing (Mitevski et al., 2021; Orbe et al., 2023). Therefore, the question of how tropospheric transport responds to increased greenhouse gas concentrations remains and needs to be explored in comprehensive climate model simulations.

Here we examine the connections between the atmospheric circulation and tracer transport response to increased CO_2, using output from abrupt $2xCO_2$ and $4xCO_2$ simulations from two versions of the "Middle Atmosphere" NASA Goddard Institute for Space Studies (GISS) climate model (E2.2-G). There are substantial differences in the large-scale circulation response both between abrupt $2xCO_2$ and $4xCO_2$ experiments and between two versions of E2.2-G. We quantify these differences and their impact on the transport from the northern midlatitude surface using passive idealized tracers.

To analyze the large-scale tropospheric transport's response to CO_2, GISS E2.2-G included synthetic tracers that were requested as a part of the Chemistry-Climate Model Initiative (CCMI, Eyring et al., 2013). These tracers have idealized sources and sinks, which enables the impact of transport to be diagnosed and compared between simulations. Here, we focus on a subset of idealized decay tracers of NH midlatitude surface origin within the troposphere. Previous studies have used these tracers to compare the transport in simulations of the current climate from multiple models (Orbe et al., 2017, 2018; Yang et al., 2019), whereas here we examine their climate change response.

The model simulations are described in Section 2, then in Section 3 we compare the climate change response between simulations, the nonlinearity in atmospheric circulation and tropospheric transport, and differences between the two model versions. Concluding remarks are in Section 4.

2 Model and Methods

We analyze output from the NASA GISS Middle Atmosphere Model E2.2 coupled with the GISS dynamical ocean model (E2.2-G), which is available on the CMIP6 archive and documented in detail in Rind et al. (2020). Briefly, the horizontal resolution of E2.2-G is 2° x 2.5° in the atmosphere and 1° in the ocean. The atmosphere consists of 102 vertical levels up to 0.002 hPa (~89 km). We examine output from two configurations of E2.2-G: one with non-interactive (NINT) chemistry, and the other with interactive aerosols and trace gases ("one-moment aerosol", OMA, Bauer et al., 2020; DallaSanta et al., 2021). In NINT simulations, only water vapor responds to CO_2 changes, while other trace gases and aerosols are held constant. In OMA simulations, aerosols and other trace gases such as stratospheric ozone also respond to CO_2 changes.

A suite of idealized tracers were included in the simulations (see Orbe et al., 2020). Here we focus on the "NH50" tracer which has a fixed mixing ratio of 10 ppm over the NH midlatitude surface (30-50°N). Above the surface, the tracer concentration χ has a single source term $-\chi/\tau_c$, where $\tau_c = 50$ days, i.e., the tracer has an e-folding decay time of 50 days. We also show briefly the response of NH5 ($\tau_c = 5$ days) which is qualitatively similar (Orbe et al., 2020).

We analyze the Pre-Industrial (PI) control and "branching" abrupt 2xCO_2 and 4xCO_2 experiments from both NINT and OMA configurations (NASA Goddard Institute for Space Studies (NASA/GISS), 2019c, 2019a, 2019b). For all experiments, we average data over the last 50 years of 150 years of simulations to represent their equilibrium states, unless specified otherwise. The difference between abrupt CO_2 and PI equilibrium states represents the estimated equilibrium response to CO_2 forcing, abbreviated as $\Delta 2xCO_2^{NINT}$, $\Delta 4xCO_2^{NINT}$, $\Delta 2xCO_2^{OMA}$, and $\Delta 4xCO_2^{OMA}$. Significance of the response is assessed by a two-sample Student's *t*-test comparing PI and abrupt CO_2 time series.

In order to highlight any nonlinearity in response, one can normalize the response by the forcing difference (Mitevski et al., 2021), or by the global-mean surface temperature response. The latter has been adopted in the IPCC AR6 (i.e., "global warming levels"), though studies have suggested that circulation responses do not always scale with the equilibrium climate sensitivity (e.g., Grise & Polvani, 2016). Here, we follow Mitevski et al. (2021) and normalize the response

by $\ln(n \times CO_2/1 \times CO_2)$, where n is 2 or 4 multiple of the PI value (Byrne & Goldblatt, 2014). We then define nonlinearity between the abrupt 2xCO_2 and 4xCO_2 experiments by $\frac{1}{2}\Delta 4 \times CO_2 - \Delta 2 \times CO_2$ for any field of interest. A similar approach was used in Orbe et al. (2020) who identified nonlinearity in the tropospheric response (e.g., the mean meridional overturning circulation) to increased CO_2. Here, we further investigate the nonlinearity in tropospheric circulation and transport.

3 Results

3.1 Surface Temperature and Jet Response

First, we highlight the differences in surface temperature response to abrupt CO_2 forcing in the NINT and OMA simulations, which is the most pronounced in NH winter (December-January-February, DJF). While the surface warming is ubiquitous in $\Delta 2xCO_2^{NINT}$ (Figure 1a), in $\Delta 4xCO_2^{NINT}$ the North Atlantic cools (Figure 1b), forming the North Atlantic warming hole (NAWH), which is a well-documented feature in GCMs (e.g., Drijfhout et al., 2012). This suggests that the surface temperature response is nonlinear to CO_2 forcing: relative to $\Delta 2xCO_2^{NINT}$, we find cooling in the NH high latitudes in $\Delta 4xCO_2^{NINT}$ (Figure 1c).

The nonlinearity in the DJF surface temperature response in the OMA simulations is weaker and of the opposite sign. The NAWH is present in both $\Delta 2xCO_2^{OMA}$ and $\Delta 4xCO_2^{OMA}$ (Figure 1d and 1e), but the normalized cooling in $\Delta 4xCO_2^{OMA}$ is less than in $\Delta 2xCO_2^{OMA}$, leading to a nonlinearity that corresponds to a warming in the North Atlantic and throughout NH high latitudes (Figure 1f).

In addition to the nonlinearity of the response to CO_2 forcing in NINT and OMA, Figures 1g and 1h also show that the surface warming for the same increase in CO_2 differ between the two model versions. Most dramatically there is surface cooling in the North Atlantic for $\Delta 2xCO_2^{OMA}$ but not $\Delta 2xCO_2^{NINT}$. The cause of this difference has been recently investigated. The comparison of NINT and OMA simulations for the same CO_2 forcing thus provides another approach to examine the impact of atmospheric circulation on transport (see Section 3.3).

Similar to surface temperature, the DJF midlatitude jet response displays pronounced differences between $\Delta 2xCO_2^{NINT}$ and $\Delta 4xCO_2^{NINT}$: the northward jet shift in the Pacific and the tripole pattern over Europe and North Africa in $\Delta 4xCO_2^{NINT}$ are absent in $\Delta 2xCO_2^{NINT}$ (Figure 2a

& 2b). This results in strong nonlinear jet response in NINT that is characterized by a poleward jet shift in both basins (Figure 2c). On the contrary, $\Delta 2xCO_2^{OMA}$ and $\Delta 4xCO_2^{OMA}$ show nearly identical patterns in the jet response (Figure 2d & 2e), resulting in weak OMA nonlinearity (Figure 2f). For a given CO_2 forcing, the difference between OMA and NINT shows a poleward shift of the Pacific jet and an equatorward shift of the Atlantic jet core (Figure 2g & 2h). This is consistent with previous studies that the NAWH can drive a poleward shift of the midlatitude jet (Gervais et al., 2019; Liu et al., 2020). Next, we analyze the zonal mean atmospheric circulation response and its effect on tracer transport.

3.2 Nonlinearity in Atmospheric Response

3.2.1 NINT Simulations

As shown in Figure 1 there are substantial differences in the DJF surface temperature response to abrupt $2xCO_2$ and $4xCO_2$ in the NINT simulations. The cooling in the NH extratropics in $4xCO_2$ relative to $2xCO_2$ extends into the Arctic lower troposphere (Figure 3f), strengthening the zonal-mean meridional temperature gradients. In the tropics and Southern Hemisphere, the nonlinearity is positive but weak throughout the troposphere.

We expect the nonlinearity in temperature response to CO_2 to result in a nonlinear response in the NH midlatitude jet and storm tracks via meridional temperature gradient changes (Figure 3f). This is indeed the case, with opposite signs of the zonal wind response on the poleward side of the jet (Figure 3g-i): There is a weakening of these winds for $\Delta 2xCO_2^{NINT}$ but a strengthening for $\Delta 4xCO_2^{NINT}$, which corresponds to slight equatorward shift of the zonal-mean jet for $\Delta 2xCO_2^{NINT}$ but a poleward shift for $\Delta 4xCO_2^{NINT}$. The difference between these two responses is a large positive anomaly north of the jet core, i.e., a large poleward jet shift associated with the surface cooling over the northern high latitudes . This poleward shift with cooling of NH high latitudes has been found in previous modeling studies examining the impact of the AMOC on the large-scale atmospheric circulation (Bellomo et al., 2021; Liu et al., 2020; Orbe et al., 2023). While there are significant differences in the zonal wind response in the NH, the differences are minimal in the SH. This is consistent with Liu et al. (2020) and Orbe et al. (2023), but not with the multi-model analysis of Bellomo et al. (2021) who found a poleward shift in the SH jet for models with larger NAWH and AMOC decline.

192 The zonal wind response is not zonally symmetric for both abrupt forcing simulations
193 (Figure 4d & 4e). In $\Delta 2xCO_2^{NINT}$, the jet weakens in the western Pacific without any clear shift,
194 while the North Atlantic jet shifts equatorward. In contrast, in $\Delta 4xCO_2^{NINT}$ there is a prominent
195 poleward jet shift in the western Pacific, which is opposite to the equatorward jet shift in the
196 North Atlantic. These differences lead to a rather zonally symmetric nonlinear response, with
197 strengthening north of 50°N and weakening south of 40°N. As the Pacific and Atlantic jets differ
198 in latitude, this corresponds to a poleward jet shift in the Pacific jet in $\Delta 4xCO_2^{NINT}$ relative to
199 $\Delta 2xCO_2^{NINT}$ but strengthening of the Atlantic jet.

200 There are also differences in the response of the mean meridional circulation between the
201 $\Delta 2xCO_2^{NINT}$ and $\Delta 4xCO_2^{NINT}$ (Figure 3j-l). Although both simulations show complex responses
202 in the DJF Eulerian-mean stream function, the nonlinearity is dominated by a strengthening of
203 the northern Hadley Cell that is strongest below 400 hPa. Previous studies have found a similar
204 Hadley Cell strengthening in response to AMOC shutdown and northern high latitude cooling
205 (R. Zhang & Delworth, 2005; Jackson et al., 2015; Orihuela-Pinto et al., 2022). The poleward
206 shift of the northern Hadley Cell edge and the northern Ferrel Cell are also consistent with a
207 poleward shift of the midlatitude jet.

208 Next, we consider the tracer response, focusing on DJF when the circulation changes are
209 the largest. As discussed in previous studies using the NH50 tracer (Wu et al., 2018; Orbe et al.,
210 2018, 2020), the climatological distribution of zonal-mean NH50 concentration in DJF is the
211 highest near the surface source region (30-50°N) and decreases more rapidly to the south than to
212 the north (contours in Figure 3a-c). In the middle to upper troposphere, the latitude of maximum
213 tracer concentration is shifted poleward (more prominently than in the annual mean), and the
214 contours of constant tracer concentration are parallel with isentropes. This is consistent with
215 isentropic mixing playing a major role in shaping the zonal mean tracer distribution.

216 For both $\Delta 2xCO_2^{NINT}$ and $\Delta 4xCO_2^{NINT}$, the NH50 response is characterized by a positive
217 anomaly in the upper troposphere in the extratropics and a negative anomaly in the middle to
218 lower troposphere (Figure 3a & 3b). Although the general pattern of NH50 response is similar,
219 there are significant differences in the location and magnitude of the negative anomaly. In
220 $\Delta 4xCO_2^{NINT}$, the negative anomaly is the most prominent directly above the source region (30-
221 50°N) from 800 to 400 hPa. However, in $\Delta 2xCO_2^{NINT}$, the most prominent negative anomaly is

found north of 50°N below 600 hPa. Furthermore, the positive anomaly near the tropopause in the midlatitudes extends deeper into the troposphere compared to the positive anomaly for $\Delta 4xCO_2^{NINT}$. Their differences are highlighted in the nonlinear NH50 response to CO_2, which is characterized by a dipole in the NH with a negative anomaly to the south of 50°N and positive to the north, with the center of the dipole following the 290 K isentrope (Figure 3c).

As with the temperature and zonal wind responses, there are noticeable zonal asymmetries in individual simulations, but the NH50 nonlinearity to CO_2 is mostly zonal in the mid-troposphere (Figure 4a-c). In $\Delta 4xCO_2^{NINT}$, there is a negative NH50 anomaly centered at the source region (30-50°N) that extends from Eurasia to the western Pacific. On the contrary, in $\Delta 2xCO_2^{NINT}$, a positive NH50 anomaly over North America is the dominant feature. The opposite signs of the NH50 response over Eurasia and North America between $\Delta 2xCO_2^{NINT}$ and $\Delta 4xCO_2^{NINT}$ give rise to the overall negative NH50 nonlinearity across midlatitudes.

The dipole pattern of the zonal-mean NH50 nonlinearity is found in the same region with the most prominent zonal wind nonlinearity (Figure 3c and i), suggesting that changes in the zonal-mean zonal wind explains the tracer transport response. Specifically, the poleward shift in the jet associated with the NAWH and northern high latitude cooling leads to the dipole pattern of NH50 in the NH extratropics. This dipole response of tracers to a jet shift is consistent with previous studies (e.g., Orbe et al., 2013, 2015). Orbe et al. (2013) linked this tracer response to a poleward shift of the eddy kinetic energy (EKE) and changes in the isentropic mixing. Nonlinearity in EKE response to CO_2, consistent with the nonlinearity in zonal winds, is also found in our simulations, with a positive EKE anomaly around 50°N associated with the NH high latitude cooling (Figure 3g-i black contours, see also Orbe et al. (2023)). If mixing occurs primarily along isentropes, the enhanced eddy mixing will increase tracer concentration north of the 290 K isentrope, as the 265-290 K contours intersect with the NH50 source region at surface (Figure 3c). On the other hand, enhanced mixing will decrease tracer concentration south of the 290 K isentrope, because these contours intersect the surface south of the tracer source region with low tracer concentration.

To further establish the relationship between zonal wind and NH50, we explore their interannual variability in the midlatitudes. We find a strong anti-correlation between DJF tropospheric-mean zonal-mean zonal wind averaged over 40-60°N and NH50 averaged over 30-

50°N for both 2xCO_2 and 4xCO_2 simulations (Figure 5a). We also find weak but significant trends: zonal wind weakens in 2xCO_2 but strengthens in 4xCO_2, while NH50 increases in 2xCO_2 but decreases in 4xCO_2 over 150 years. The interannual correlations remain significant after detrending the data: about 60% of the interannual variability of NH50 can be explained by zonal wind variability in 2xCO_2, while the amount increases to 65% in 4xCO_2 (Figure 5b). The passive nature of the NH50 tracer allows us to establish a causality where zonal winds drive the variability of NH50 on an interannual timescale in the midlatitudes.

While the extratropical response is the most prominent, there is also a significant nonlinearity in the NH50 response in the tropical lower troposphere (Figure 3a-c). This is consistent with the NH Hadley cell expansion in the evident nonlinear overturning stream function response to CO_2 (Figure 3j-l). In $\Delta 4xCO_2^{NINT}$, the Hadley Cell edge lies closer to the middle of the source region (i.e., 40N), resulting in larger near-surface equatorward transport by the Eulerian mean circulation into the tropics. Tropical convection effectively transports anomalous tracers upward and across the equator. This Hadley Cell-transport relationship is consistent with Yang et al. (2019, 2020), who showed that the transport of tracers away from a midlatitude surface source is sensitive to the location of the Hadley Cell edge.

As noted above there is a positive NH50 anomaly near the extratropical tropopause in both $\Delta 2xCO_2^{NINT}$ and $\Delta 4xCO_2^{NINT}$ (Figure 3a & 3b). This positive anomaly does not appear in the nonlinearity, indicating that the NAWH and northern high latitude cooling does not play a major role here. The positive anomaly can largely be explained by increased tropopause height (e.g., Abalos et al., 2017). The tropopause height is expected to increase under increased CO_2 concentrations due to both tropospheric warming and stratospheric cooling (Vallis et al., 2015). As the NH50 concentration decreases strongly with height in the upper troposphere and lower stratosphere, an increase in the tropopause results in an increase in tracer at fixed pressure. To quantify this effect, we follow the analysis in Abalos et al. (2017) and remap NH50 onto tropopause-relative coordinates by redefining vertical levels as distance to the tropopause for each simulation (Figure A1). In $\Delta 4xCO_2^{NINT}$, the positive anomaly near the tropopause is removed and only the negative anomaly remains after remapping, consistent with Abalos et al. (2017). The difference in normalized NH50 response between $\Delta 4xCO_2^{NINT}$ and $\Delta 2xCO_2^{NINT}$ after

remapping still shows a dipole pattern (cf. Figure 3), suggesting that tropopause rise is not the main cause of NH50 nonlinearity.

3.2.2 OMA Simulations

We now examine the nonlinearity and the dependency of tracer transport response on the midlatitude jet in the OMA simulations. As discussed in Section 3.1, both $\Delta 2xCO_2^{OMA}$ and $\Delta 4xCO_2^{OMA}$ have a more extensive NAWH than in $\Delta 4xCO_2^{NINT}$. However, there is noticeable nonlinearity in surface temperatures, which is of the opposite sign to the NINT nonlinearity (Figure 1).

As for the NINT, the nonlinearity in surface temperature extends into the lower troposphere in OMA. There is also warming in the Arctic lower stratosphere in the OMA nonlinearity (Figure 6f). Consistent with the opposite sign in temperature nonlinearity, the sign of the OMA atmospheric circulation nonlinearity is also opposite to that of the NINT. Specifically, the nonlinear response in OMA corresponds to a weakening of winds on the poleward side and a strengthening on the equatorward side (an equatorward shift) of the jet (Figure 6f), while the jet shift is poleward in NINT nonlinearity (Figure 3f). There is also a contraction of the NH Hadley Cell edge in OMA that is opposite to NINT (Figure 6l). Consistent with the arguments above regarding the tracer response to the shift in the jet and Hadley Cell edge, the nonlinearity in the NH50 response in OMA is opposite to that in NINT (Figure 6c and Figure 4c). The magnitude of the nonlinearity in atmospheric circulation and tracer response are weaker in OMA than in NINT, further supporting the hypothesis that the tracer response is determined primarily by the meridional movement of the atmospheric circulation.

3.3 OMA–NINT Differences

As discussed in Section 3.1, the response of surface temperature and the midlatitude jet for the same CO_2 forcing differs between the OMA and NINT simulations. In particular, there is a prominent NAWH for $\Delta 2xCO_2^{OMA}$ but not for $\Delta 2xCO_2^{NINT}$. This creates an alternative way to examine the jet-transport connections. Specifically, we repeat the above analysis but rather than focusing on the nonlinearity to CO_2 forcing, we compare the $2xCO_2$ and $4xCO_2$ response between OMA and NINT (two configurations of the same model under the same CO_2 forcing).

The general characteristics of $\Delta 2xCO_2^{OMA}$ (left column of Figure 6) are similar to those for $\Delta 4xCO_2^{NINT}$ (middle column of Figure 3), with negligible Arctic amplification, a poleward shift of the midlatitude jet, and a decrease in NH50 in the middle-upper troposphere above the source region. As a result, $\Delta 2xCO_2^{OMA}$–$\Delta 2xCO_2^{NINT}$ for different fields closely resembles the NINT nonlinearity (Figure 7a, c). Specifically, there is cooling above the Arctic surface, a poleward shift of the jet, and decreased transport into the middle-upper troposphere above the source region but increased transport poleward of the source region. This pattern of NH50 response is rather zonally symmetric (Figure 4c, g). The EKE response for $\Delta 2xCO_2^{OMA}$–$\Delta 2xCO_2^{NINT}$ also looks similar to NINT nonlinearity (and resembles the $\Delta 2xCO_2^{OMA}$–$\Delta 2xCO_2^{NINT}$ zonal wind response), and thus support the conclusion that changes in eddy mixing along isentropes drives the tracer response. Furthermore, the Hadley Cell response for $\Delta 2xCO_2^{OMA}$–$\Delta 2xCO_2^{NINT}$ shows a poleward expansion in the NH, leading to an increase in NH50 in the tropical lower troposphere (not shown). The above supports our main finding that a poleward shift in the NH jet and Hadley cell edge can lead to a dipole response in tracers of mid-latitude origin.

The $\Delta 4xCO_2^{OMA}$–$\Delta 4xCO_2^{NINT}$ fields also support this finding. The same dipole response in NH50 can be seen in $\Delta 4xCO_2^{OMA}$–$\Delta 4xCO_2^{NINT}$, which is again connected to a poleward shift of the jet and EKE and Arctic cooling (Figure 7). This can further be connected to the stronger cooling of the Arctic surface in the OMA $4xCO_2$ simulation (Figure 1e).

The similarity between $\Delta 2xCO_2^{OMA}$–$\Delta 2xCO_2^{NINT}$, $\Delta 4xCO_2^{OMA}$–$\Delta 4xCO_2^{NINT}$, and NINT nonlinearity is a surprising result. Although OMA-NINT highlights the impact of interactive chemistry while NINT nonlinearity highlights the nonlinear response to CO_2 forcing, both show the NAWH and northern high latitude cooling. It emphasizes the potential role ocean dynamics play in shaping the long-term climate change response, which we discuss in Section 3.4. The northern high latitude cooling leads to strengthened meridional temperature gradients in the troposphere, accompanied by the strengthening of the zonal wind and EKE on the poleward flank of the NH jet. This leads to increased eddy mixing along isentropes and reduced tracer concentration in the midlatitudes, which applies to all combinations of simulations.

3.3 Other Tracers

So far, we have focused on a single idealized passive tracer NH50 to diagnose the changes in transport. This raises the issue of robustness of the results for other tracers, with differing sources or chemical loss. Very similar results are found for other idealized CCMI tracers, including NH5 and the age from NH midlatitudes (AOA-NH, see Figure 13 of Orbe et al., 2020), but here we consider additional tracers which not only differ in their lifetime, but also in their sources or sinks.

The boundary condition for NH50 is fixed mixing ratios within the source region, but a more realistic boundary condition is fixed emissions. To test the sensitivity to the choice of boundary conditions the NH50 and a new NH50-emissions tracer (same loss but boundary condition of fixed emissions in same source region) have been included in a NINT 6xCO_2 simulation. There is no corresponding NH50-emissions tracer in a NINT PI run, so we diagnose the response of both tracers as the difference between the first and last 10 years in the 6xCO_2 simulation (Figure 8). The NH50 response for the 6xCO_2 resembles that for $\Delta 4xCO_2^{NINT}$ (Figure 8a, consistent with the above finding that the response pattern is similar whenever the NAWH is present). More importantly, the NH50-emissions response is also similar. There are differences near the source region, which is expected given that the mixing of NH50-emissions can change in the source region but NH50 mixing ratio is fixed. However, the pattern away from the source region is very similar, with decrease above the source region and increase in Arctic and tropical lower troposphere (Figure 8b). This suggests that the conclusions drawn from the NH50 tracer also hold for tracers with fixed emissions.

We can also take advantage of the OMA simulations that include full chemistry to explore the changes in more realistic chemical tracers. Figure 9 shows $\Delta 2xCO_2^{OMA}$ response of sulfur dioxide (SO_2) and industrially-sourced black carbon (BC), averaged over years 131-150. These species have main sources in the NH extratropics and lifetime of 4-12 days for BC and longer for SO_2. We also include NH5, which has a shorter lifetime of 5 days that is more relevant for BC. For both BC and SO_2, there is a decrease in their concentrations in northern mid-latitudes and an increase in northern high latitudes. While the detailed structures differ between these tracers and the passive tracers, there is considerable agreement in the general structures between NH5 and BC/SO_2. The dipole response is consistent with the changes in transport diagnosed above from NH50. Specifically, the poleward shift of the jet results in increased midlatitude eddy

mixing, leading to reduced tracer concentration in the mid-latitudes but increased concentration in the Arctic.

3.4 **AMOC Response**

Finally, we hypothesize that the difference in AMOC evolution can lead to different jet and tracer transport responses in the GISS E2.2-G simulations. Under abrupt 4xCO2 forcing, CMIP5/6 models with larger AMOC decline have a more poleward shift of the midlatitude jet than models with smaller AMOC decline (Bellomo et al., 2021). Freshwater hosing experiment further demonstrates that AMOC weakening can cause the NAWH and a poleward shift of the midlatitude jet (Liu et al., 2020). Although establishing the causality between the AMOC and the midlatitude jet is beyond the scope of this paper, we show a consistent relationship in the GISS E2.2-G suite.

Figure 1 highlights the presence of the NAWH in all but $\Delta 2xCO_2^{NINT}$. Indeed, the evolution of AMOC (defined by the maximum meridional overturning stream function at 48°N) shows prominent weakening in all abrupt CO2 simulations except for $\Delta 2xCO_2^{NINT}$, where an initial weakening of 5 Sv is followed by rapid recovery in the first 35 years (Figure 10a). Consequently, we find a strong nonlinearity in the NINT AMOC response. The AMOC weakens throughout the abrupt $4xCO_2$ simulation and $\Delta 4xCO_2^{NINT}$ is -10 Sv, which results in a nonlinearity of -5 Sv to CO2 forcing in the NINT simulations.

On the other hand, the AMOC response in OMA simulations is rather linear to CO_2 forcing: the AMOC response is -7 Sv and -17 Sv in $\Delta 2xCO_2^{OMA}$ and $\Delta 4xCO_2^{OMA}$ respectively (Figure 10b). Furthermore, the AMOC reaches a total collapse in the last 50 years of the OMA abrupt $4xCO_2$ simulation. The AMOC nonlinearity is only -1.5 Sv in OMA simulations, which is significantly weaker than the nonlinearity in NINT.

For both abrupt 2xCO2 and 4xCO2, OMA simulations consistently have larger AMOC weakening than NINT simulations have. Previous study has shown that under abrupt CO2 forcing, the stratospheric ozone induces an equatorward shift of the North Atlantic jet in DJF (Chiodo & Polvani, 2019). The resulting negative North Atlantic Oscillation pattern can lead to AMOC weakening (Delworth & Zeng, 2016). Although the details of the mechanism in OMA simulations are still being investigated, it is manifested in cooler surface temperatures in NH high latitudes (Figure 1g & 1h) and a poleward shift of the midlatitude jet (Figure 7g & 7h).

Although the NAWH may not be entirely caused by AMOC weakening, the impacts of NAWH on the midlatitude jet are robust (Gervais et al., 2019). Therefore, we expect the different AMOC behavior in NINT and OMA to have a significant impact on atmospheric circulation and tracer transport because of the longer response time scale of ocean dynamics compared to the atmosphere. 4 Summary and Conclusions

In order to understand how tracer transport responds to climate change, we utilize a series of abrupt CO_2 forcing simulations using the NASA GISS Climate Model E2.2-G that include a passive tracer emitted at northern midlatitudes with a 50 day^{-1} loss rate (NH50). We find that the equilibrium response of NH50 to CO_2 forcing is dependent on the response of the midlatitude jet in boreal winter. This connection is found in individual abrupt CO_2 simulations, the nonlinearity of the response to CO_2 forcing in each model, and the difference between models (Figure 7). In cases of a poleward shift of the midlatitude jet, we find a zonal-mean dipole pattern consisting of a negative NH50 anomaly in the midlatitudes and a positive NH50 anomaly in the Arctic troposphere (Figure 11). This occurs because the jet shift is associated with enhanced EKE on the poleward flank of the jet, which increases isentropic eddy mixing of low NH50 air from the subtropical surface to the midlatitude upper troposphere and high NH50 air from the midlatitude surface to the Arctic troposphere. In the tropics, the response of NH50 is sensitive to the shift in the NH Hadley Cell edge and its associated mean meridional circulation. Our findings are consistent with earlier works by Orbe et al. (2013, 2015), who employed a different modeling approach of air-mass fractions to show a similar relationship between midlatitude jet, eddy mixing, and tracer transport in response to increased greenhouse gases.

The nonlinearity of the circulation and NH50 responses to CO_2 forcing differs between the two configurations of the GISS E2.2-G model: There is substantial nonlinearity in NINT (non-interactive chemistry where only water vapor responds to CO_2 forcing) but only weak nonlinearity in OMA (interactive chemistry). We trace this to differences in surface temperature response in NH high latitudes. This temperature change is highly nonlinear in NINT, with the presence of NAWH in $\Delta 4xCO_2^{NINT}$ but not in $\Delta 2xCO_2^{NINT}$. Consequently, the nonlinear surface temperature response leads to a poleward shift of the midlatitude jet. The NH50 zonal-mean nonlinear response to CO_2 in NINT is characterized by a dipole pattern of negative anomaly in the midlatitude and positive anomaly in the Arctic in boreal winter. In OMA, on the other hand, the NAWH is present and the northern midlatitude jet moves poleward in both abrupt $2xCO_2$ and

430 $4xCO_2$ simulations. The NH50 response shows little OMA nonlinearity to CO_2 forcing as a
431 result.

432 The DJF jet-tracer relationship is also found in the difference between OMA and NINT
433 simulations with the same CO_2 forcing. For both abrupt $2xCO_2$ and $4xCO_2$, the OMA simulation
434 shows stronger North Atlantic cooling and weaker warming in northern high latitudes than in
435 NINT simulations. Consequently, the meridional temperature gradient is strengthened more in
436 OMA simulations, leading to a more poleward shift of the midlatitude jet and a dipole NH50
437 response in the zonal mean.

438 The surprising similarity between $\Delta 2xCO_2^{OMA} - \Delta 2xCO_2^{NINT}$ and NINT nonlinearity
439 highlights the importance of ocean dynamics in shaping the long-term climate change response
440 in the atmosphere. In both cases, weaker AMOC corresponds to a more poleward shift of the NH
441 midlatitude jet, a relationship that is also found in different ensemble members under the same
442 radiative forcing (Orbe et al., 2023). Despite using a different modeling approach, our findings
443 are consistent with Erukhimova et al. (2009) who showed a similar dipole response to AMOC
444 weakening for parcels released in the midlatitude lower troposphere. Although Erukhimova et al.
445 (2009) mainly focused on inter-hemispheric transport, they also suggested the importance of
446 isentropic mixing due to eddies in dispersing parcels in the extratropics.

447 While our analysis has focused on a single idealized passive tracer, with fixed mixing
448 ratio boundary condition and uniform loss rate, the key results hold for tracers with flux
449 boundary conditions and variable chemical loss, including simulations of sulfur dioxide and
450 black carbon. Specifically, for tracers with midlatitude surface sources, the poleward shift of the
451 jet and its enhanced midlatitude eddy mixing lead to reduced tracer concentration in the
452 midlatitudes but increased concentration in the Arctic. Thus, the climate change response of the
453 jet has the potential to modify the concentrations of tracer gases and aerosols in mid and high
454 latitudes without any changes in emissions, and subsequently affect both atmospheric chemistry
455 and radiative balance. More research is needed to quantify these impacts.

456 **Appendix**

457 **Figure A1** DJF zonal mean NH50 response from NINT simulations after adjusting for
458 tropopause changes, following Abalos et al. (2017). NH50 PI climatology is shown in gray

459 contours. Solid black lines show PI tropopause height. Dashed black lines show abrupt CO_2
460 tropopause height.

461 **Acknowledgments**

462 We thank two anonymous reviewers for their constructive comments. Climate modeling at GISS
463 is supported by the NASA Modeling, Analysis and Prediction program, and resources supporting
464 this work were provided by the NASA High-End Computing (HEC) Program through the NASA
465 Center for Climate Simulation (NCCS) at Goddard Space Flight Center. This work was funded
466 by support from the US National Science Foundation (NSF) and the National Aeronautics and
467 Space Administration (NASA).

468 **Open Research**

469 The GISS E2.2-G temperature (*tas*, *ta*), zonal wind (*ua*), ocean overturning streamfunction
470 (*msftmz*) data used in the study are available at the CMIP6 archive via the Earth System Grid
471 Federation (https://esgf-node.llnl.gov/). The specific simulations used here are the piControl,
472 abrupt-2xCO2, and abrupt-4xCO2 r1i1p1f1 (NINT) and r1i1p3f1 (OMA) runs (NASA Goddard
473 Institute for Space Studies (NASA/GISS), 2019c, 2019a, 2019b). Tracers, atmospheric
474 overturning streamfunction, EKE, and tropopause height data are available at
475 https://doi.org/10.6084/m9.figshare.22492810.
476

References

Abalos, M., Randel, W. J., Kinnison, D. E., & Garcia, R. R. (2017). Using the Artificial Tracer e90 to Examine Present and Future UTLS Tracer Transport in WACCM. *Journal of the Atmospheric Sciences*, *74*(10), 3383–3403. https://doi.org/10.1175/JAS-D-17-0135.1

Bauer, S. E., Tsigaridis, K., Faluvegi, G., Kelley, M., Lo, K. K., Miller, R. L., Nazarenko, L., Schmidt, G. A., & Wu, J. (2020). Historical (1850–2014) Aerosol Evolution and Role on Climate Forcing Using the GISS ModelE2.1 Contribution to CMIP6. *Journal of Advances in Modeling Earth Systems*, *12*(8), e2019MS001978. https://doi.org/10.1029/2019MS001978

Bellomo, K., Angeloni, M., Corti, S., & von Hardenberg, J. (2021). Future climate change shaped by inter-model differences in Atlantic meridional overturning circulation response. *Nature Communications*, *12*(1), Article 1. https://doi.org/10.1038/s41467-021-24015-w

Byrne, B., & Goldblatt, C. (2014). Radiative forcing at high concentrations of well-mixed greenhouse gases. *Geophysical Research Letters*, *41*(1), 152–160. https://doi.org/10.1002/2013GL058456

Chiodo, G., & Polvani, L. M. (2019). The Response of the Ozone Layer to Quadrupled CO2 Concentrations: Implications for Climate. *Journal of Climate*, *32*(22), 7629–7642. https://doi.org/10.1175/JCLI-D-19-0086.1

DallaSanta, K., Orbe, C., Rind, D., Nazarenko, L., & Jonas, J. (2021). Dynamical and Trace Gas Responses of the Quasi-Biennial Oscillation to Increased CO2. *Journal of Geophysical Research: Atmospheres*, *126*(6), e2020JD034151. https://doi.org/10.1029/2020JD034151

Delworth, T. L., & Zeng, F. (2016). The Impact of the North Atlantic Oscillation on Climate through Its Influence on the Atlantic Meridional Overturning Circulation. *Journal of Climate*, *29*(3), 941–962. https://doi.org/10.1175/JCLI-D-15-0396.1

Doherty, R. M., Orbe, C., Zeng, G., Plummer, D. A., Prather, M. J., Wild, O., Lin, M., Shindell, D. T., & Mackenzie, I. A. (2017). Multi-model impacts of climate change on pollution transport from global emission source regions. *Atmospheric Chemistry and Physics*, *17*(23), 14219–14237. https://doi.org/10.5194/acp-17-14219-2017

Drijfhout, S., van Oldenborgh, G. J., & Cimatoribus, A. (2012). Is a Decline of AMOC Causing the Warming Hole above the North Atlantic in Observed and Modeled Warming Patterns? *Journal of Climate*, *25*(24), 8373–8379. https://doi.org/10.1175/JCLI-D-12-00490.1

Erukhimova, T., Zhang, R., & Bowman, K. P. (2009). The climatological mean atmospheric transport under weakened Atlantic thermohaline circulation climate scenario. *Climate Dynamics*, *32*(2), 343–354. https://doi.org/10.1007/s00382-008-0402-x

Eyring, V., Lamarque, J.-F., Hess, P., Arfeuille, F., Bowman, K., Chipperfield, M. P., Duncan, B., Fiore, A., Gettelman, A., Giorgetta, M. A., Granier, C., Hegglin, M., Newman, P. A., Peter, T., Robock, A., Ryerson, T., Saiz-Lopez, A., Salawitch, R., Schulz, M., … Waugh, D. W. (2013). Overview of IGAC/SPARC Chemistry-Climate Model Initiative (CCMI) Community Simulations in Support of Upcoming Ozone and Climate Assessments. *SPARC Newsletter*, *40*, 48–66.

Gervais, M., Shaman, J., & Kushnir, Y. (2019). Impacts of the North Atlantic Warming Hole in Future Climate Projections: Mean Atmospheric Circulation and the North Atlantic Jet. *Journal of Climate*, *32*(10), 2673–2689. https://doi.org/10.1175/JCLI-D-18-0647.1

Grise, K. M., & Polvani, L. M. (2016). Is climate sensitivity related to dynamical sensitivity? *Journal of Geophysical Research: Atmospheres*, *121*(10), 5159–5176. https://doi.org/10.1002/2015JD024687

He, C., Clement, A. C., Cane, M. A., Murphy, L. N., Klavans, J. M., & Fenske, T. M. (2022). A North Atlantic Warming Hole Without Ocean Circulation. *Geophysical Research Letters*, *49*(19), e2022GL100420. https://doi.org/10.1029/2022GL100420

Jackson, L. C., Kahana, R., Graham, T., Ringer, M. A., Woollings, T., Mecking, J. V., & Wood, R. A. (2015). Global and European climate impacts of a slowdown of the AMOC in a high resolution GCM. *Climate Dynamics*, *45*(11), 3299–3316. https://doi.org/10.1007/s00382-015-2540-2

Keil, P., Mauritsen, T., Jungclaus, J., Hedemann, C., Olonscheck, D., & Ghosh, R. (2020). Multiple drivers of the North Atlantic warming hole. *Nature Climate Change*, *10*(7), Article 7. https://doi.org/10.1038/s41558-020-0819-8

Liu, W., Fedorov, A. V., Xie, S.-P., & Hu, S. (2020). Climate impacts of a weakened Atlantic Meridional Overturning Circulation in a warming climate. *Science Advances*, *6*(26), eaaz4876. https://doi.org/10.1126/sciadv.aaz4876

Mitevski, I., Orbe, C., Chemke, R., Nazarenko, L., & Polvani, L. M. (2021). Non-Monotonic Response of the Climate System to Abrupt CO2 Forcing. *Geophysical Research Letters*, *48*(6), e2020GL090861. https://doi.org/10.1029/2020GL090861

Monks, S. A., Arnold, S. R., Emmons, L. K., Law, K. S., Turquety, S., Duncan, B. N., Flemming, J., Huijnen, V., Tilmes, S., Langner, J., Mao, J., Long, Y., Thomas, J. L., Steenrod, S. D., Raut, J. C., Wilson, C., Chipperfield, M. P., Diskin, G. S., Weinheimer, A., … Ancellet, G. (2015). Multi-model study of chemical and physical controls on transport of anthropogenic and biomass burning pollution to the Arctic. *Atmospheric Chemistry and Physics*, *15*(6), 3575–3603. https://doi.org/10.5194/acp-15-3575-2015

NASA Goddard Institute for Space Studies (NASA/GISS). (2019a). *NASA-GISS GISS-E2-2-G model output prepared for CMIP6 CFMIP abrupt-2xCO2 [dataset]* (Version 20191120). Earth System Grid Federation. https://doi.org/10.22033/ESGF/CMIP6.11688

NASA Goddard Institute for Space Studies (NASA/GISS). (2019b). *NASA-GISS GISS-E2-2-G model output prepared for CMIP6 CMIP abrupt-4xCO2 [dataset]* (Version 20191120). Earth System Grid Federation. https://doi.org/10.22033/ESGF/CMIP6.6978

NASA Goddard Institute for Space Studies (NASA/GISS). (2019c). *NASA-GISS GISS-E2-2-G model output prepared for CMIP6 CMIP piControl [dataset]* (Version 20191120). Earth System Grid Federation. https://doi.org/10.22033/ESGF/CMIP6.7382

Orbe, C., Holzer, M., Polvani, L. M., & Waugh, D. (2013). Air-mass origin as a diagnostic of tropospheric transport. *Journal of Geophysical Research: Atmospheres*, *118*(3), 1459–1470. https://doi.org/10.1002/jgrd.50133

Orbe, C., Newman, P. A., Waugh, D. W., Holzer, M., Oman, L. D., Li, F., & Polvani, L. M. (2015). Air-mass Origin in the Arctic. Part II: Response to Increases in Greenhouse Gases. *Journal of Climate*, *28*(23), 9105–9120. https://doi.org/10.1175/JCLI-D-15-0296.1

Orbe, C., Rind, D., Jonas, J., Nazarenko, L., Faluvegi, G., Murray, L. T., Shindell, D. T., Tsigaridis, K., Zhou, T., Kelley, M., & Schmidt, G. A. (2020). GISS Model E2.2: A Climate Model Optimized for the Middle Atmosphere—2. Validation of Large-Scale Transport and Evaluation of Climate Response. *Journal of Geophysical Research: Atmospheres*, *125*(24), e2020JD033151. https://doi.org/10.1029/2020JD033151

Orbe, C., Rind, D., Miller, R. L., Nazarenko, L., Romanou, A., Jonas, J., Russell, G., Kelley, M., & Schmidt, G. (2023). Atmospheric Response to a Collapse of the North Atlantic Circulation Under A Mid- Range Future Climate Scenario: A Regime Shift in Northern Hemisphere Dynamics. *Journal of Climate*.

Orbe, C., Waugh, D. W., Yang, H., Lamarque, J.-F., Tilmes, S., & Kinnison, D. E. (2017). Tropospheric transport differences between models using the same large-scale meteorological fields. *Geophysical Research Letters*, *44*(2), 1068–1078. https://doi.org/10.1002/2016GL071339

Orbe, C., Yang, H., Waugh, D. W., Zeng, G., Morgenstern, O., Kinnison, D. E., Lamarque, J.-F., Tilmes, S., Plummer, D. A., Scinocca, J. F., Josse, B., Marecal, V., Jöckel, P., Oman, L. D., Strahan, S. E., Deushi, M., Tanaka, T. Y., Yoshida, K., Akiyoshi, H., … Banerjee, A. (2018). Large-scale tropospheric transport in the Chemistry–Climate Model Initiative (CCMI) simulations. *Atmospheric Chemistry and Physics*, *18*(10), 7217–7235. https://doi.org/10.5194/acp-18-7217-2018

Orihuela-Pinto, B., England, M. H., & Taschetto, A. S. (2022). Interbasin and interhemispheric impacts of a collapsed Atlantic Overturning Circulation. *Nature Climate Change*, *12*(6), Article 6. https://doi.org/10.1038/s41558-022-01380-y

Oudar, T., Cattiaux, J., & Douville, H. (2020). Drivers of the Northern Extratropical Eddy-Driven Jet Change in CMIP5 and CMIP6 Models. *Geophysical Research Letters*, *47*(8), e2019GL086695. https://doi.org/10.1029/2019GL086695

Rahmstorf, S., Box, J. E., Feulner, G., Mann, M. E., Robinson, A., Rutherford, S., & Schaffernicht, E. J. (2015). Exceptional twentieth-century slowdown in Atlantic Ocean overturning circulation. *Nature Climate Change*, *5*(5), 475–480. https://doi.org/10.1038/nclimate2554

Rind, D., Orbe, C., Jonas, J., Nazarenko, L., Zhou, T., Kelley, M., Lacis, A., Shindell, D., Faluvegi, G., Romanou, A., Russell, G., Tausnev, N., Bauer, M., & Schmidt, G. (2020). GISS Model E2.2: A Climate Model Optimized for the Middle Atmosphere—Model Structure, Climatology, Variability, and Climate Sensitivity. *Journal of Geophysical Research: Atmospheres*, *125*(10), e2019JD032204. https://doi.org/10.1029/2019JD032204

Shaw, T. A. (2019). Mechanisms of Future Predicted Changes in the Zonal Mean Mid-Latitude Circulation. *Current Climate Change Reports*, *5*(4), 345–357. https://doi.org/10.1007/s40641-019-00145-8

Shaw, T. A., Baldwin, M., Barnes, E. A., Caballero, R., Garfinkel, C. I., Hwang, Y.-T., Li, C., O'Gorman, P. A., Rivière, G., Simpson, I. R., & Voigt, A. (2016). Storm track processes and the opposing influences of climate change. *Nature Geoscience*, *9*(9), 656–664. https://doi.org/10.1038/ngeo2783

Shepherd, T. G. (2014). Atmospheric circulation as a source of uncertainty in climate change projections. *Nature Geoscience*, *7*(10), Article 10. https://doi.org/10.1038/ngeo2253

Shindell, D. T., Chin, M., Dentener, F., Doherty, R. M., Faluvegi, G., Fiore, A. M., Hess, P., Koch, D. M., MacKenzie, I. A., Sanderson, M. G., Schultz, M. G., Schulz, M., Stevenson, D. S., Teich, H., Textor, C., Wild, O., Bergmann, D. J., Bey, I., Bian, H., … Zuber, A. (2008). A multi-model assessment of pollution transport to the Arctic. *Atmospheric Chemistry and Physics*, *8*(17), 5353–5372. https://doi.org/10.5194/acp-8-5353-2008

Vallis, G. K., Zurita-Gotor, P., Cairns, C., & Kidston, J. (2015). Response of the large-scale structure of the atmosphere to global warming. *Quarterly Journal of the Royal Meteorological Society*, *141*(690), 1479–1501. https://doi.org/10.1002/qj.2456

Wu, X., Yang, H., Waugh, D. W., Orbe, C., Tilmes, S., & Lamarque, J.-F. (2018). Spatial and temporal variability of interhemispheric transport times. *Atmospheric Chemistry and Physics*, *18*(10), 7439–7452. https://doi.org/10.5194/acp-18-7439-2018

Yang, H., Waugh, D. W., Orbe, C., & Chen, G. (2020). Dependence of Atmospheric Transport Into the Arctic on the Meridional Extent of the Hadley Cell. *Geophysical Research Letters*, *47*(20), e2020GL090133. https://doi.org/10.1029/2020GL090133

Yang, H., Waugh, D. W., Orbe, C., Zeng, G., Morgenstern, O., Kinnison, D. E., Lamarque, J.-F., Tilmes, S., Plummer, D. A., Jöckel, P., Strahan, S. E., Stone, K. A., & Schofield, R. (2019). Large-scale transport into the Arctic: The roles of the midlatitude jet and the Hadley Cell. *Atmospheric Chemistry and Physics*, *19*(8), 5511–5528. https://doi.org/10.5194/acp-19-5511-2019

Zhang, R., & Delworth, T. L. (2005). Simulated Tropical Response to a Substantial Weakening of the Atlantic Thermohaline Circulation. *Journal of Climate*, *18*(12), 1853–1860. https://doi.org/10.1175/JCLI3460.1

Zhang, X., Waugh, D. W., & Orbe, C. (2023). *Dependence of Northern Hemisphere Tropospheric Transport on the Midlatitude Jet under Abrupt CO2 Increase [Dataset]*. figshare. https://doi.org/10.6084/m9.figshare.22492810

635 **Figure 1** DJF surface air temperature response for NINT (a) 2xCO_2, (b) 4xCO_2, (c) nonlinearity,
636 and OMA (d) 2xCO_2, (e) 4xCO_2, (f) nonlinearity. Differences between OMA and NINT
637 responses are shown on (g) for 2xCO_2 and (h) for 4xCO_2.

638 **Figure 2** Same as Figure 1 but for DJF zonal wind at 850 hPa. Contours show PI climatological
639 zonal wind with intervals of 5 m/s.

640 **Figure 3** DJF zonal mean response from NINT simulations. (a)-(c) NH50; (d)-(f) temperature;
641 (g)-(i) zonal wind and EKE (black contours with intervals of 10 m^2/s^2); (j)-(l) Eulerian mean
642 overturning stream function. Gray contours show PI climatology with contour intervals of (a)-(c)
643 1ppm; (d)-(f) 10 K; (g)-(i) 10 m/s; and (j)-(l) 2×10^{10} kg/s. PI climatology of potential
644 temperature is shown in black contours on (c). Tracer source region is shown by the black bar
645 near the surface. Regions that do not have statistically significant response at 95% level are
646 hatched.

647 **Figure 4** Same as Figure 1 but for DJF NH50 at 700 hPa. *Dashed lines indicate 30°N and 50°N.*

648 **Figure 5** DJF zonal wind and NH50 relationship in NINT simulations. (a) Time series of
649 vertically averaged (1000-200 hPa) zonal mean NH50 at 30-50°N (solid) and zonal wind at 40-
650 60°N (dashed). A 10-year running mean filter has been applied to all fields. Note the NH50 axis
651 has been flipped. Black dashed line and gray shading show the mean and +/- one standard
652 deviation of the PI zonal wind. (b) Scatter plot of NH50 and zonal wind as in (a). Solid dots
653 show detrended data with their correlation coefficients shown. Transparent dots show data
654 without detrending.

655 **Figure 6** Same as Figure 3 but for OMA simulations.

656 **Figure 7** Same as Figure 1 but for Northern Hemispheric DJF zonal mean response of NH50
657 (colors) and zonal wind (contours start from 0.5 m/s in solid and -0.5 m/s in dashed with 1 m/s
658 intervals).

659 **Figure 8** DJF NH50 response in NINT abrupt 6xCO_2 simulation (defined as the difference
660 between years 141-150 and 1-10). (a) NH50 with fixed mixing ratio at 30-50°N surface. Gray

661 contours show PI climatology with intervals of 1 ppm. (b) NH50 with fixed emission (flux) at
662 30-50°N surface. Gray contours show PI climatology with intervals of 0.1 ppm.

663 **Figure 9** DJF response to 2xCO_2 in OMA simulations. (a) NH50, (b) SO_2, and (c) industrially-
664 sourced black carbon, all in ppm. Gray contours show the climatology with intervals of 0.5 ppm.

665 **Figure 10** Annual-mean AMOC strength (defined as the maximum Atlantic overturning stream
666 function at 48°N) time series from (a) NINT and (b) OMA simulations.

667 **Figure 11** Schematic of the DJF jet-tracer responses in the troposphere. A poleward shift of the
668 midlatitude jet (black contours) is associated with enhanced eddy mixing (wavy arrows) along
669 isentropes (gray contours). This leads to more mixing of low tracer concentration air from the
670 tropical surface (white wavy arrows) and high tracer concentration air from the midlatitude
671 surface (black wavy arrows), which results in a dipole tracer anomaly. Tracer source region is
672 shown by the black bar.

Figure 1.

(a) NINT Δ2xCO2

(b) NINT Δ4xCO2

(c) NINT nonlinearity

(d) OMA Δ2xCO2

(e) OMA Δ4xCO2

(f) OMA nonlinearity

(g) Δ2xCO2 OMA-NINT

(h) Δ4xCO2 OMA-NINT

16
12
8
4
0
−4
−8
−12
−16
[K]

Figure 2.

(a) NINT Δ2xCO2

(b) NINT Δ4xCO2

(c) NINT nonlinearity

(d) OMA Δ2xCO2

(e) OMA Δ4xCO2

(f) OMA nonlinearity

(g) Δ2xCO2 OMA-NINT

(h) Δ4xCO2 OMA-NINT

4
3
2
1
0
−1
−2
−3
−4
[m/s]

Figure 3.

(a) NINT Δ2xCO2
(b) NINT Δ4xCO2
(c) NINT Nonlinearity
(d)
(e)
(f)
(g)
(h)
(i)
(j)
(k)
(l)
Pressure [hPa]
Latitude
NH50 [ppm]
Temperature [K]
Zonal Wind [m/s]
1e9
Streamfunction [kg/s]

Figure 4.

(a) NINT Δ2xCO2

(b) NINT Δ4xCO2

(c) NINT nonlinearity

(d) OMA Δ2xCO2

(e) OMA Δ4xCO2

(f) OMA nonlinearity

(g) Δ2xCO2 OMA-NINT

(h) Δ4xCO2 OMA-NINT

0.6
0.4
0.2
0.0
−0.2
−0.4
−0.6
[ppm]

Figure 5.

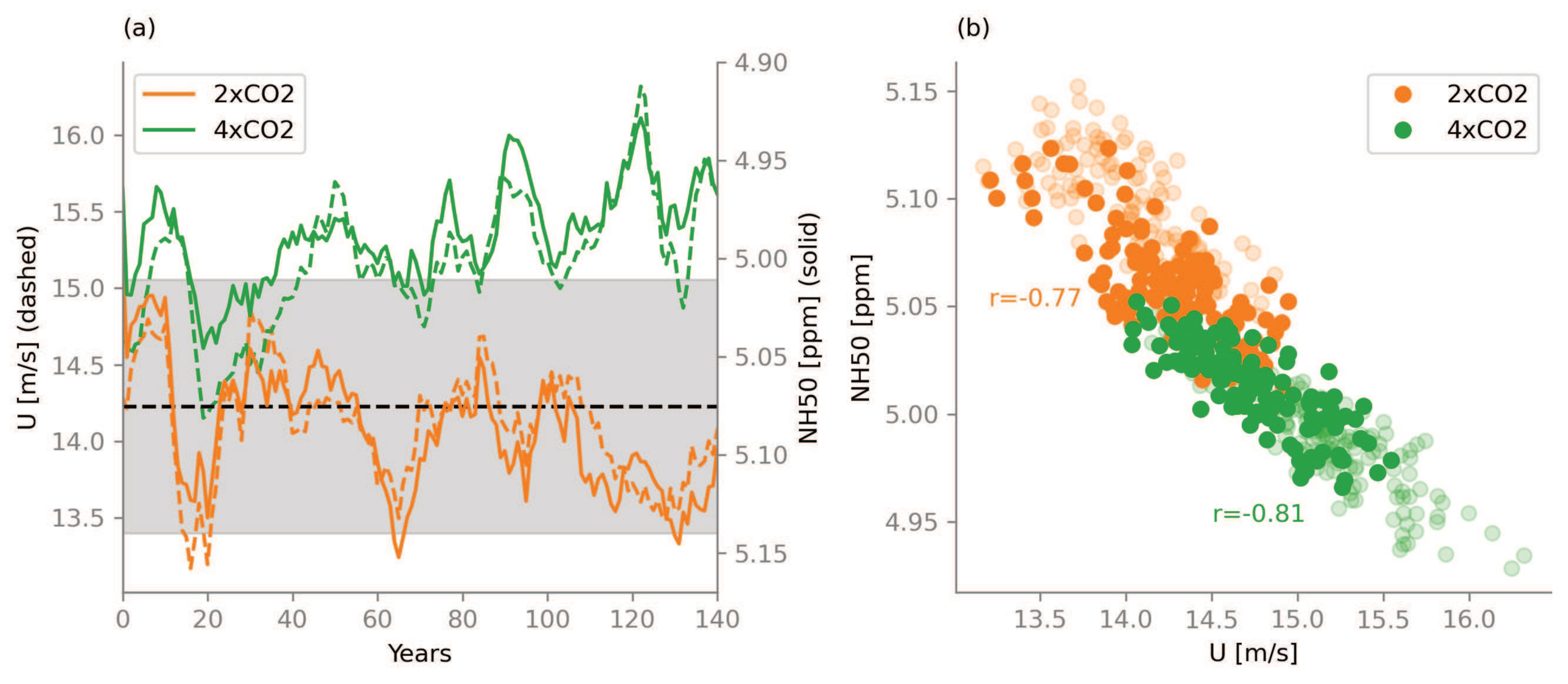
(a)
2xCO2
4xCO2
U [m/s] (dashed)
NH50 [ppm] (solid)
Years
16.0
15.5
15.0
14.5
14.0
13.5
4.90
4.95
5.00
5.05
5.10
5.15
0
20
40
60
80
100
120
140
(b)
2xCO2
4xCO2
r=-0.77
r=-0.81
NH50 [ppm]
U [m/s]
5.15
5.10
5.05
5.00
4.95
13.5
14.0
14.5
15.0
15.5
16.0

Figure 6.

(a) OMA Δ2xCO2
(b) OMA Δ4xCO2
(c) OMA Nonlinearity
(d)
(e)
(f)
(g)
(h)
(i)
(j)
(k)
(l)
Pressure [hPa]
200
400
600
800
−50
0
50
Latitude
320
290
280
310
300
270
250
NH50 [ppm]
0.3
0.2
0.1
0.0
−0.1
−0.2
−0.3
Temperature [K]
6
4
2
0
−2
−4
−6
Zonal Wind [m/s]
4
2
0
−2
−4
1e9
Streamfunction [kg/s]
8
4
0
−4
−8

Figure 7.

(a) NINT Δ2xCO2

(b) NINT Δ4xCO2

(c) NINT nonlinearity

(d) OMA Δ2xCO2

(e) OMA Δ4xCO2

(f) OMA nonlinearity

(g) Δ2xCO2 OMA-NINT

(h) Δ4xCO2 OMA-NINT

Pressure (hPa)

200
400
600
800

0
25
50
75

Latitude

0.4
0.2
0.0
−0.2
−0.4

[ppm]

Figure 8.

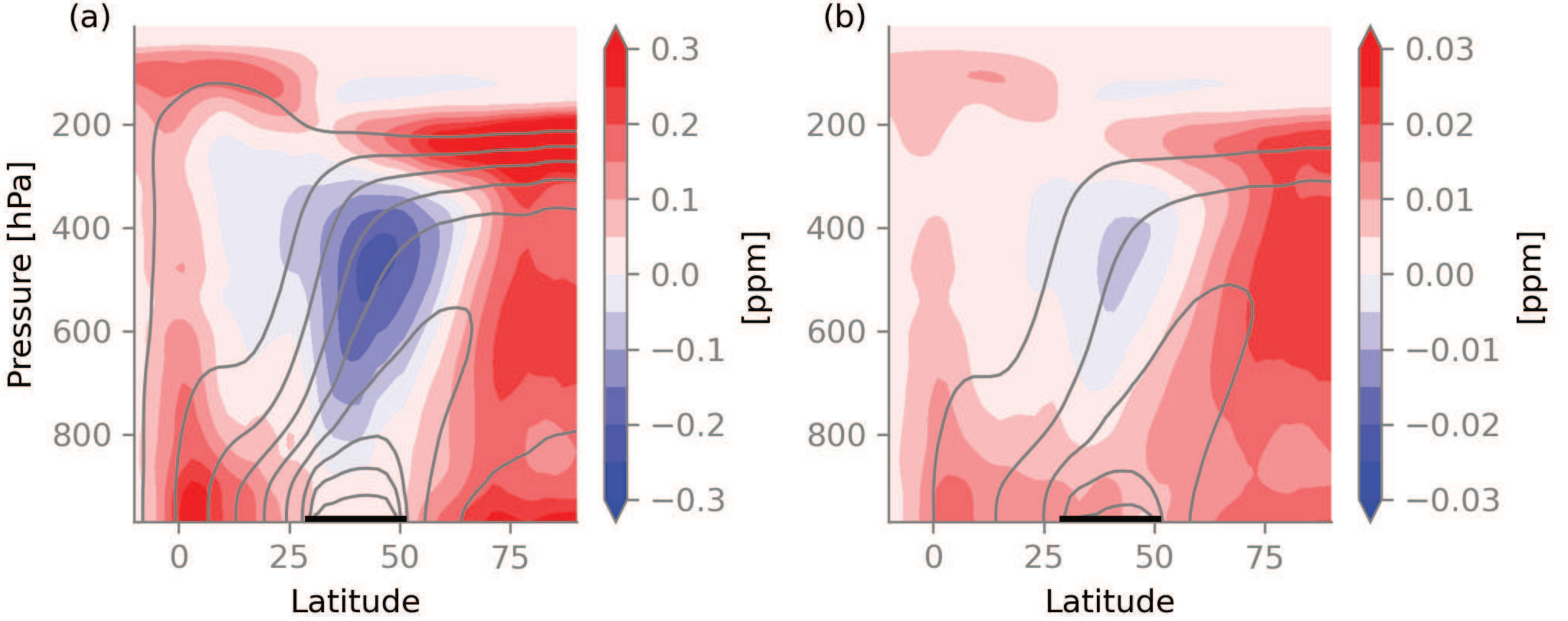
(a)
(b)
Pressure [hPa]
200
400
600
800
0
25
50
75
Latitude
0.3
0.2
0.1
0.0
−0.1
−0.2
−0.3
[ppm]
0.03
0.02
0.01
0.00
−0.01
−0.02
−0.03

Figure 9.

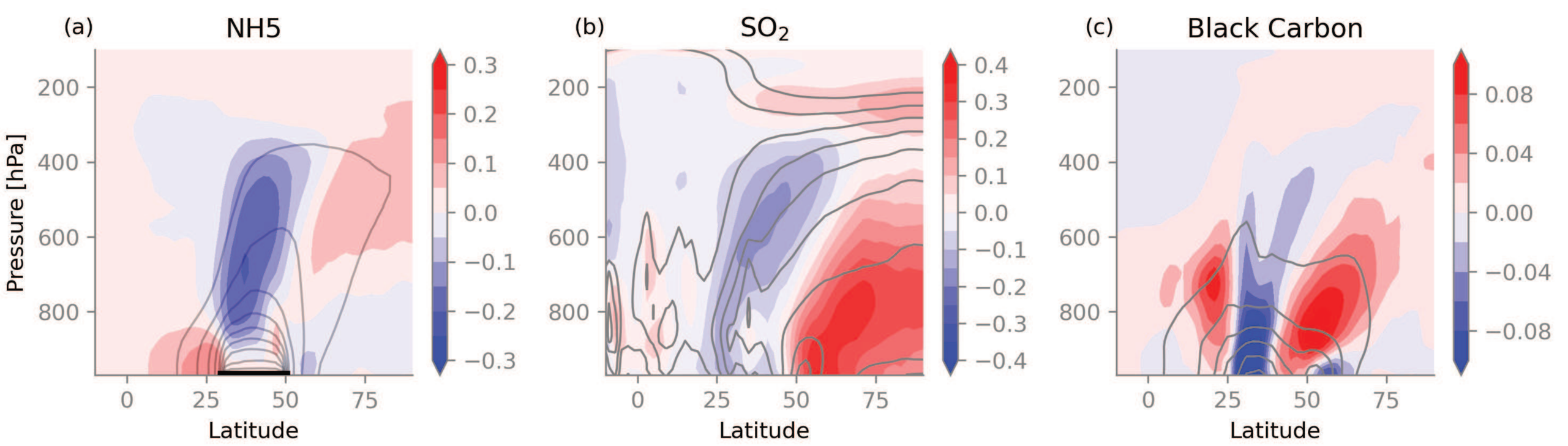
(a)
NH5
(b)
SO_2
(c)
Black Carbon
Pressure [hPa]
200
400
600
800
0
25
50
75
Latitude
0.3
0.2
0.1
0.0
−0.1
−0.2
−0.3
0.4
0.3
0.2
0.1
0.0
−0.1
−0.2
−0.3
−0.4
0.08
0.04
0.00
−0.04
−0.08

Figure 10.

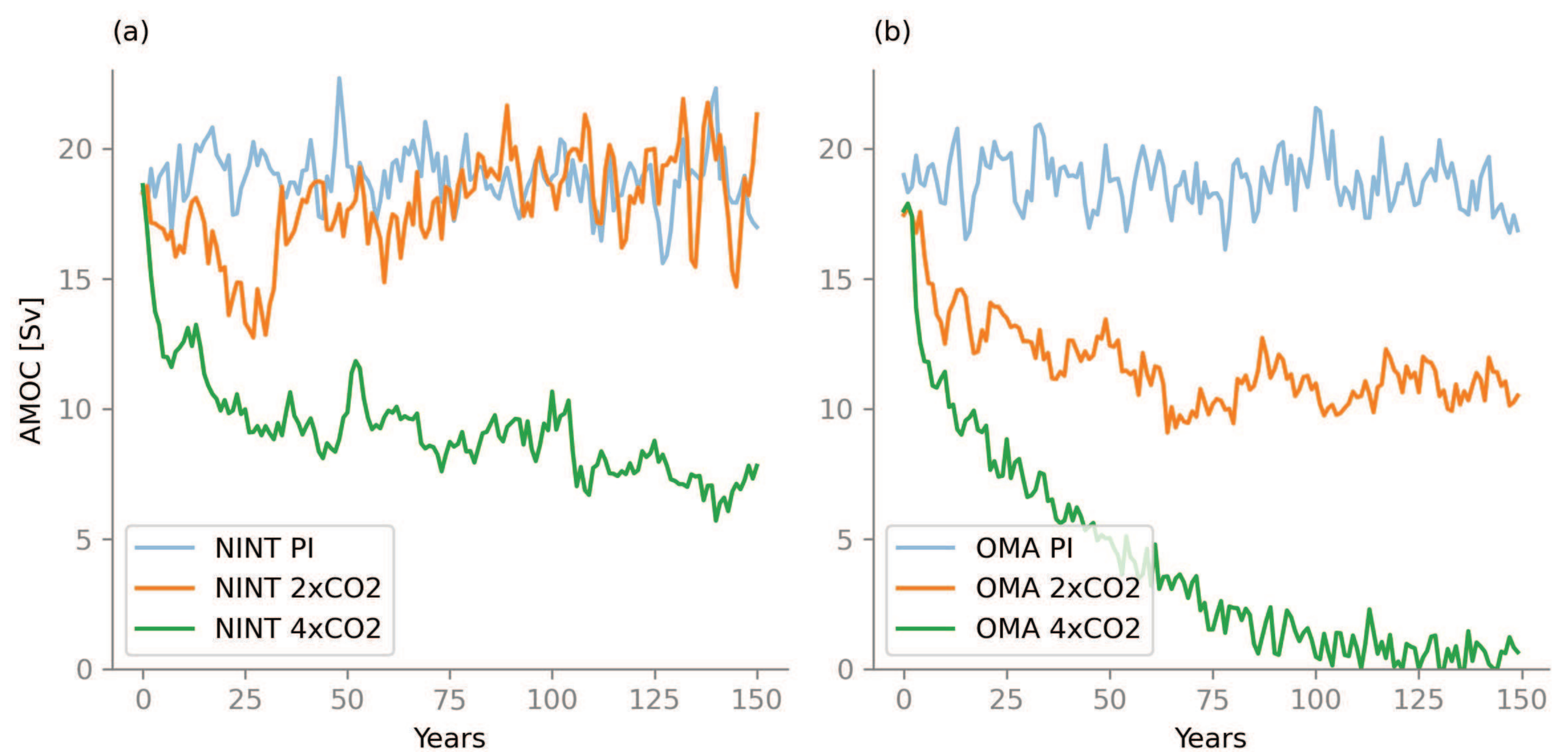
(a)
(b)
AMOC [Sv]
0
5
10
15
20
0
25
50
75
100
125
150
Years
NINT PI
NINT 2xCO2
NINT 4xCO2
OMA PI
OMA 2xCO2
OMA 4xCO2

Figure 11.

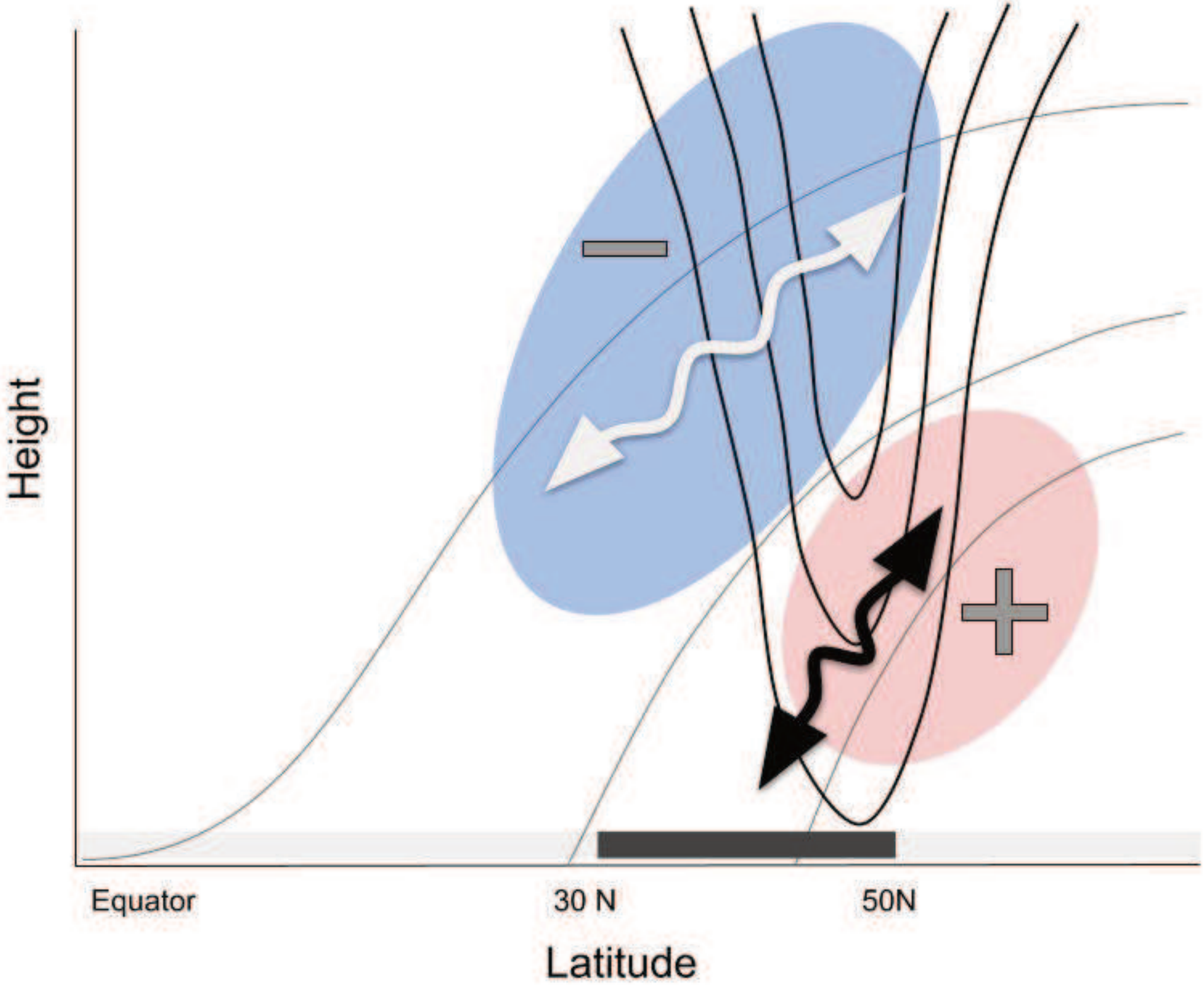
Height
Equator
30 N
50N
Latitude

Figure A1.

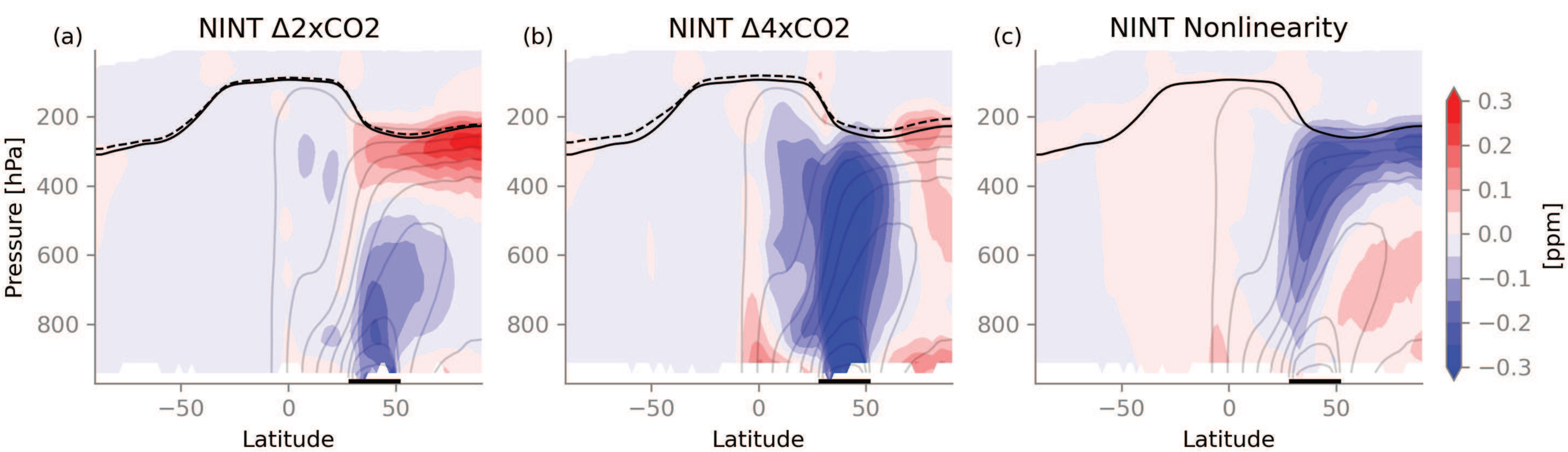
(a)
NINT Δ2xCO2
(b)
NINT Δ4xCO2
(c)
NINT Nonlinearity
Pressure [hPa]
200
400
600
800
−50
0
50
Latitude
0.3
0.2
0.1
0.0
−0.1
−0.2
−0.3
[ppm]